PAPER

Check for updates

Thermomorphological and mechanical properties of vulcanized octenyl succinate/terpenoid-derivatized corn starch composites†

Moira K. Lauer,[a] Andrew G. Tennyson [ID] [ab] and Rhett C. Smith [ID] *[a]

Modification of food starches with octenyl succinic anhydride (OSA) is a well-established protocol to endow the starches with olefin moieties that can subsequently undergo traditional polyolefin crosslinking and polymerization reactions. In the current work, olefin-modified starch derivatives are crosslinked with sulfur, through reactions mechanistically similar to vulcanization of the olefin moieties in rubber, thus yielding the analogous vulcanized starch composites. Given the importance of the olefin moieties in the vulcanization mechanism, OSA-modified corn starch was further derivatized by esterification with geraniol, a terpenol diene. The resulting geraniol-esterified starch (**GES**) thus contains three olefin moieties per esterified site, affording double the number of crosslinkable-carbon atoms compared to typical OSA-modified starches. **GES** was reacted with elemental sulfur to generate composites **GSS$_x$** (where x = wt% sulfur, either 90 or 95 in this work). The thermomorphological and mechanical properties of **GSS$_x$** were assessed by thermogrametric analysis (TGA), differential scanning calorimetry (DSC), scanning electron microscopy with element mapping by energy-dispersive X-ray analysis (SEM-EDX), mechanical test stand analysis, and dynamic mechanical analysis (DMA) and compared to those of previously-reported composites of OSA-modified starch and elemental sulfur (**OSS$_x$**). These tests revealed that **GSS$_x$** underwent significant intramolecular crosslinking to form particles that were well-dispersed in the sulfur-rich networks of the composites. As a result, **GSS$_x$** materials behaved as particle-reinforced network materials that deformed entirely plastically before breaking under a compressional stress. In contrast, **OSS$_x$** composites exhibited longer crosslinking chains and more interaction between domains. The result of these morphological differences confers upon **GSS$_x$** lower stiffness and greater strength relative to their **OSS$_x$** analogues.

Introduction

Largely unchecked CO_2 emissions have been linked to globally increasing temperatures that foreshadow potentially devastating impacts.[1] One of the most significant contributors to both anthropogenic CO_2 and the destruction of the environment through mining is in the production of Portland cement. It is currently estimated that cement production accounts for 30% of global materials utilization and 8% of anthropogenic CO_2 production.[2] These statistics can be attributed to current concrete formulations that incorporate massive amounts of cement

clinker. Clinker is environmentally deleterious as it is produced by first mining mineral carbonates and then converting them to their respective oxides. This process requires heating the carbonates to more than 1400 °C with concomitant production of stoichiometric CO_2. This already gargantuan CO_2 output is only forecast to increase in response to current increases in annual cement production[3] to meet increasing needs for infrastructure in second and third world countries. These trends coupled with limited ability to recycle end-of-life concrete has only relatively recently led to a significant uptick in research to develop sustainable replacements for cement. Fortunately, this work has borne a variety of innovative approaches and concrete formulations to decrease our reliance on cement clinker. The majority of mineral cements, however, are still inherently acid-sensitive and environmentally vulnerable. One of the primary pitfalls of mineral cements is their high water-uptake and consequent freeze–thaw cycle-induced fissure. This paired with an inability to readily recycle cement at scale renders even these improved formulations as significant waste streams.

[a] Department of Chemistry, Clemson University, Clemson, South Carolina, 29634, USA. E-mail: rhett@clemson.edu

[b] Department of Materials Science and Engineering, Clemson University, Clemson, South Carolina, 29634, USA

† Electronic supplementary information (ESI) available: Additional synthetic and characterization including PXRD data, IR spectra, NMR spectra, TGA and DSC data, details on calculations and mechanical testing. See DOI: https://doi.org/10.1039/d1ma01202a
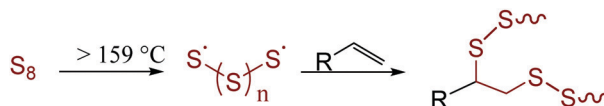
Fig. 1 Inverse vulcanization of an olefin with sulfur.

Sulfur cements were identified over a century ago for their potential to provide the structural integrity of traditional cements but with improved environmental resistance.[4–19] Early formulations of sulfur cements were formed by the vulcanization of petrochemical olefins with elemental sulfur to form a hot-set cement to which traditional fines (like sand) and aggregates (like gravel) could be added. Vulcanization – called inverse vulcanization when the reaction involved a majority wt% sulfur (Fig. 1) – involves reaction between thermally-generated oligo/polysulfur radicals with olefins.[20–25] Recently, more sustainable high sulfur-content materials (HSMs) have been prepared by vulcanizing bio-derived olefins with elemental sulfur. Such HSMs hold promise for a variety of applications including as adsorbents for environmental remediation,[26–32] as IR transparent lenses,[33–39] and in lithium sulfur batteries.[40–48] The practical application potential for HSMs has also been expanded by advances in novel processing and recycling strategies that have allowed for expanded substrate scope, lower reaction temperatures and solvent- or heat-assisted healable materials.[23,49–56] Most pertinent to the current work, however, is that many HSMs possess strength characteristics on par with or better than current cement products, yet the HSMs can be readily reshaped by simple melt-cast processes at moderate temperatures (120–180 °C).[57–61] The formulation of HSMs from sulfur – itself a by-product of petroleum refining – and an olefinic by-product of agronomic endeavours makes them attractive candidates for valorization of underutilized good to replace cement. Some of the especially promising bio-derived components of HSMs include derivatives of cellulose,[57,62] lignin,[58,63–65] mixed lignocellulosic biomass,[58,59,66] corn starch,[66,67] terpenoids,[39,57,61,68–71] triglycerides, and fatty acids.[72–74]

We recently reported materials in which modified corn starch was the organic component of HSMs.[66] In the United States alone, corn has been produced in gigaton quantities (~14–15 Gt) annually since 2013, yet its selling price has fallen by over 50% in the last ten years due to dwindling demand.[75,76] Valorisation of corn products therefore presents an exciting economic opportunity. In our previous study, corn starch was modified with octenyl succinic anhydride to prepare **OS** (degree of substitution = 2.63 ± 0.05%, Fig. 2 and 3) by the established route. Inverse vulcanization of **OS** with sulfur led to composites **OSS$_x$** (x = wt% of sulfur in the feed ratio). The **OSS$_x$** composites exhibited exceptionally long oligosulfur crosslinks between starch chains, endowing the composites with high flexural strength relative to the majority of previously-reported HSMs. Accessing biopolymer-HSMs having good mechanical properties while requiring only a low degree of biopolymer substitution is attractive because it minimizes the non-bio-derived content in the final product. Given the promising properties of **OSS$_x$** composites, we used a green modification protocol to further derivatize **OS** and to evaluate the utility of the resultant starch derivative, **GES**, as a component of starch/sulfur vulcanized composites, **GSS$_x$**. Starch derivative **OS** was thus esterified by its reaction with geraniol, a terpenoid alcohol bearing two vulcanizable olefin units, to give **GES**. This esterification was 100% atom-economical, employing L-leucine as a catalyst and geraniol as the solvent.[57] **GES** was then vulcanized with elemental sulfur to generate composite materials **GSS$_x$** (Fig. 3, x = wt% sulfur in monomer feed). The **GSS$_x$** composites exhibited significantly different morphological and mechanical characteristics relative to the **OSS$_x$** analogues.

Results and discussion

Modification of OS

Starch derivative **GES** was prepared from the same lot of **OS** (Fig. 2) that was used to prepare previously-prepared
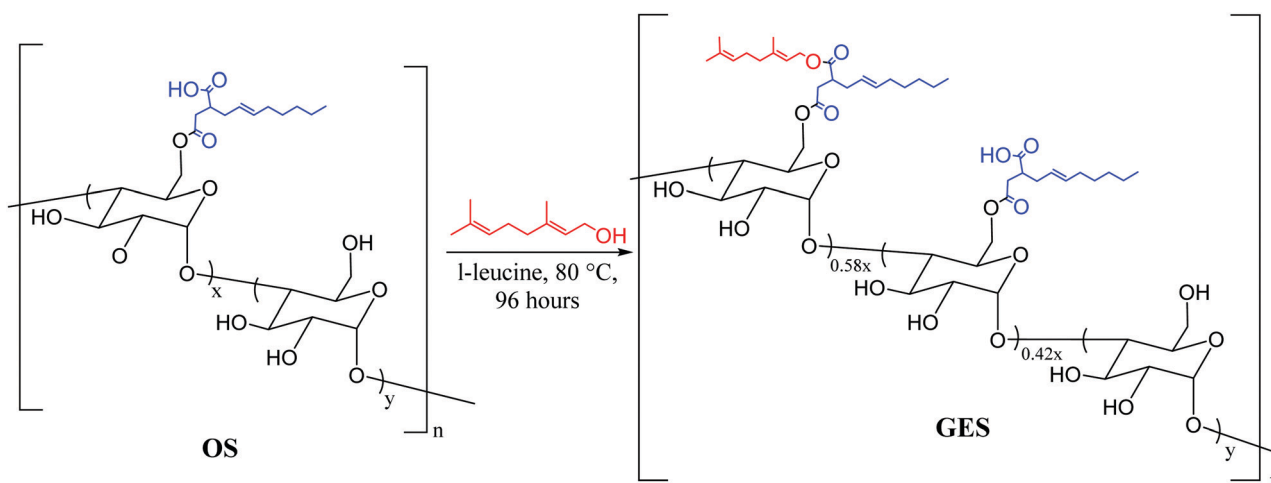

Fig. 2 Modification of **OS** with geraniol to generate **GES**. The octenyl succinate ester is highlighted in blue and the geraniol portion is in red. The values for x and y are 2.6% and 97.4%, respectively. Upon reaction, 58% of the free carboxylic acid groups are esterified with geraniol.
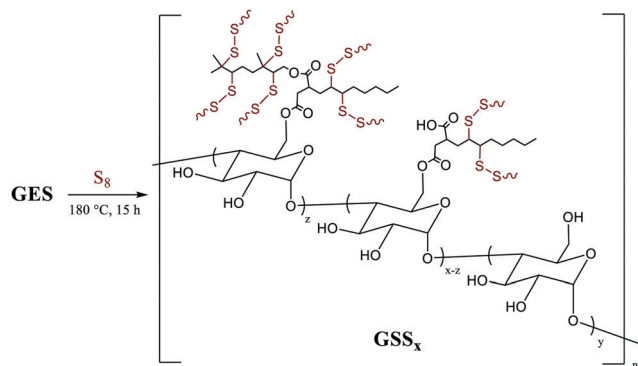
Fig. 3   Reaction of **GES** with sulfur to generate GSS_x composites (where x = wt% sulfur in the feed ratio, either 90 or 95).
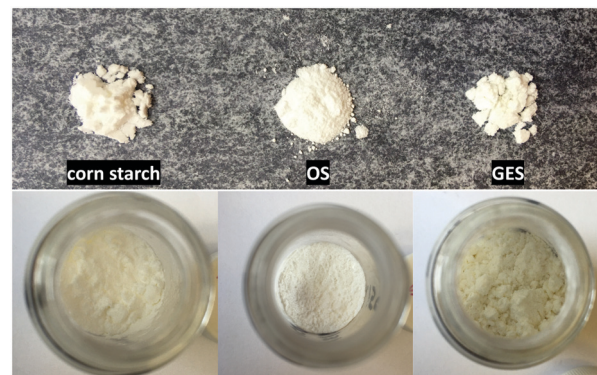

Fig. 4   Unmodified corn starch (left), **OS** (center), and **GES** (right) shown as either a pile of powder (top images) or the top-down view of a vial full of material (bottom images) showing the significant differences in physical properties.

composites OSS_x to allow direct comparison of composite properties (*vide infra*).[66] In **OS**, 2.6% of the monomer units have been substituted by their reaction with octenyl succinate to leave a carboxylic acid moiety amenable to esterification. The esterification protocol was based on our previously-reported procedure for the esterification of oxidized cellulose with geraniol.[57] Briefly, **OS** was suspended in an excess of geraniol with catalytic L-leucine. The reaction was carried out in a sealed vessel held at 80 °C for 4 days while stirring. **GES** was readily isolated by simple filtration and washing with a small amount of ethanol. The purified product was dried in a vacuum oven at 40 °C for 3 days. As in previous studies, excess geraniol was recovered and re-used without changes in its purity (as assessed by GC analysis). The esterification process is thus near 100% atom economy with small amounts of water being produced as a by-product and the green solvent ethanol was the only other compound used in the purification step. Each site esterified by its reaction with geraniol will have three times as many olefin units for crosslinking in the subsequent vulcanization step. The difference in physical properties of the starch derivatives was striking. The difference in bulk starch granule agglomeration following esterification and drying to constant mass was evident to the naked eye. Corn starch presents as clustered granules that are free flowing but can be easily pressed into a thin sheet, whereas **OS** was a very fine powder and **GES** looked more similar to corn starch than **OS** but tended to agglomerate into larger clusters of starch (Fig. 4).

Esterification of starch by this protocol increased its crystallinity to nearly the same crystallinity observed for native corn starch, an important consideration given that biopolymer crystallinity has been shown to affect changes in the mechanical properties of composites made by biopolymer vulcanization and that modification tends to decrease biopolymer crystallinity.[57] Powder X-ray diffraction (PXRD) of all three materials – corn starch starting material, **OS** and **GES** – exhibit the pattern typical of waxy corn starches that exhibit A-type crystallinity.[77] A detailed analysis of structural features contributing to A-type biopolymer crystallinity has been reported previously.[78] In the current study, the unmodified corn starch, **OS**, and **GES** were found by PXRD to have percent crystallinities of 20.9, 15.8, and 20.2%, respectively (Fig. S1 in the ESI,†). These data reveal a decrease of crystallinity

of only 0.7% over the two steps and a small increase of 4.4% upon esterification of **OS**.

Infrared (IR) spectroscopic data for **OS** and **GES** were, unsurprisingly, nearly identical (ESI,† Fig. S2). The presence of geraniol in **GES** could be qualitatively visualized in its ¹H NMR spectrum, where peaks attributable to the methyl groups of geraniol were visible at 1.64 and 1.57 ppm. Most of the other expected resonances attributable to geraniol were obscured by resonances attributable to the starch backbone and the chain of the octenyl succinate functionality (ESI,† Fig. S3). The degree of geraniol-esterification could not be determined with a high degree of certainty from either the ¹H NMR spectrum or other solution-based methods due to the limited solubility of **GES** and the small degree of substitution in the **OS** precursor. The degree of geraniol esterification was thus determined based on analysis of the thermal decomposition profile of **GES** from thermogravimetric analysis (TGA) wherein decomposition of geraniol can be observed shortly before the primary decomposition observed for the carbohydrate backbone (see ESI,† Fig. S4, S5, eqn (S1) and Table S1 for full details of the calculation). This analysis revealed that $1.5 \pm 0.2\%$ of starch monomers contain the geraniol-esterified unit, while $1.1\% \pm 0.2\%$ remain in the carboxylic acid form (Fig. 2), equating to successful esterification of 58% of sites available in parent **OS**. The result is that **GES** (0.33 mmol olefin g⁻¹) has approximately twice as many olefin units available for vulcanization with sulfur compared to **OS** (0.16 mmol olefin g⁻¹).

Both starch derivatives **OS** and **GES** possessed thermal characteristics quite similar to those of native corn starch. The decomposition of **GES** proceeded quite similarly to **OS** with the exception of the decomposition of the geraniol side chain (from ~150–230 °C), which additionally led to a slightly lower char yield for **GES** (~1.2% difference in char at 800 °C, see ESI,† Fig. S4). Differential scanning calorimetry (DSC) data revealed that both derivatives possessed T_g values slightly lower than native corn starch's T_g of 98.4 °C. Interestingly, the T_g for **GES** (97.5 °C) was slightly increased relative to **OS** (89.6 °C), indicating that the pendant geraniol chain hindered segmental chain movement relative to the free carboxylic acid group (ESI,†

Fig. S6 and Table S2), which is also consistent with the afore-mentioned trends in crystallinity observed by PXRD. Whereas there was a 9 °C drop in T_g upon modification of native starch to form **OS**, positive changes in the crystallinity of **OS** upon esterification actually improved the T_g.

Synthesis and properties of GSS_x composites

Composites **GSS$_x$** (x = wt% sulfur) were readily prepared by simply heating **GES** with elemental sulfur to initiate the inverse vulcanization reaction (Fig. 1). The reaction of **GES** with sulfur (Fig. 3) to generate **GSS$_{95}$** and **GSS$_{90}$** required longer heating at 180 °C ($\sim$15 hours) compared to that required to prepare **OSS$_x$** materials ($\sim$9 hours) due to significant agglomeration of **GES** powder at the reaction interface. This phenomenon is likely a result of strong intermolecular forces present in the granular structure and higher crystallinity of **GES** compared to **OS**. In all cases the materials were heated under nitrogen to minimize the potential for undesired oxidation reactions. Following reaction, the molten composites were poured into cuboid or cylinder-shaped silicone molds to produce samples appropriate for subsequent mechanical analysis. HSMs often contain meta-stable polysulfur catenates that take time to relax to their ultimate allotropic form. Many HSMs are therefore analyzed after 3–4 days of curing. In the current case, **GSS$_x$** materials were analyzed after 15 days of curing to match conditions employed for analysis of previously-reported **OSS$_x$** materials.

Thermal analysis of **GSS$_x$** revealed some interesting results. Both materials possessed two thermal features in the thermo-gravimetric analysis (TGA) curves. The first feature is attributable to the sublimation of S_8 (T_{sub}), while the second step is attributable to thermal degradation of the organic portion of the composite. In **GSS$_{90}$**, T_{sub} of S_8 in **GSS$_{90}$** was slightly depressed relative to **GSS$_{95}$** as the organic portion of the composite essentially acts as an 'impurity', disrupting the crystallinity and lowering T_{sub} (ESI,† Fig. S7). **GSS$_{90}$** also, unsurprisingly, showed a larger step for the decomposition of the organic portion of the material at $\sim$300 °C. In contrast to most previous HSMs, the char yield of the two **GSS$_x$** composites did not scale with the amount of organic material in the composite.[57,62] Although **GSS$_{90}$** contained less than twice (7.6 and 12.5 wt% organic for **GSS$_{95}$** and **GSS$_{90}$**, respectively, ESI,† Table S3) as much organic/crosslinkable material by elemental microanalysis, its char yield was more than three times that observed in **GSS$_{95}$**, revealing that a more thermally resistant crosslinked network forms when **GSS$_{90}$** undergoes thermal decomposition. Further evidence for higher-density crosslinking was observed in the heating and cooling curves obtained by DSC for **GSS$_x$**. Whereas **GSS$_{95}$** exhibited thermo-morphological changes quite similar to those observed for pure sulfur (*i.e.*, sulfur melting feature on heating and recrystalliza-tion on cooling), **GSS$_{90}$** exhibited a reversible T_g at −40 °C, a feature never before observed for biopolymer–sulfur compo-sites except for sulfur composites prepared from lignin with quite high degrees of crosslinking (Fig. 5).[58,63–65] Crystallization on cooling is unsurprisingly delayed (requires cooling to a lower temperature) for **GSS$_{90}$** relative to **GSS$_{95}$** by more than
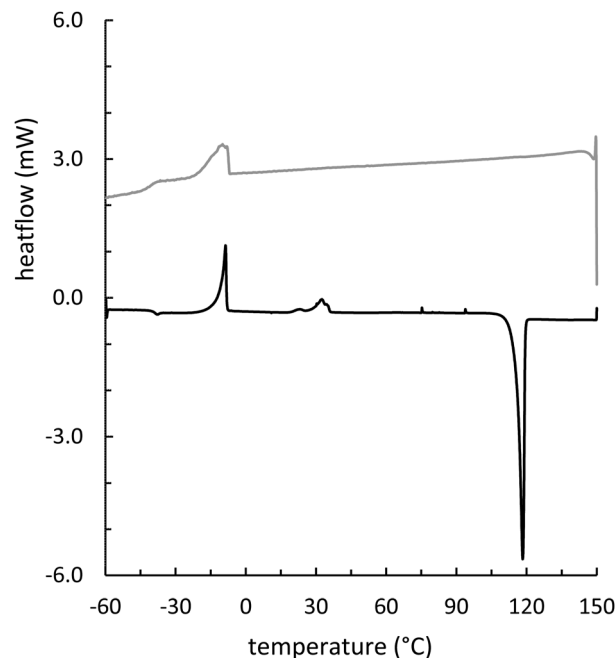

Fig. 5 DSC heating (black) and cooling (gray) curves from the third cycle for **GSS$_{90}$**. The intensity of the cooling cycle has been multiplied by 4 and shifted by +1.2 mW to make the features appear more prominent. The heating cycle shows a T_g for polymeric sulfur with a midpoint at −39 °C. Two regions of cold crystallization are visible at −24 to −1 °C and from 18 to 39 °C. The melting endotherm for $S_8(\beta)$ appears at 118 °C. In the cooling cycle, a crystallization exotherm occurs at −12 °C and the reversible T_g is apparent with midpoint at −41 °C.

25 °C and numerous cold-crystallization features are observed upon heating (ESI,† Fig. S8 and S9). These data provide further evidence that the crosslinked portion of **GSS$_{90}$** is more robust and likely contains more highly crosslinked material with shorter sulfur catenates bridging biopolymer crosslinks compared to **GSS$_{95}$**.

To better understand the differences in crosslinking in the two **GSS$_x$** materials, each was subjected to fractionation with CS_2. This is a common technique for extracting any noncovalently-bound sulfur, which is readily soluble in CS_2, from an HSM to leave behind only the organosulfur network in the insoluble fraction. Based on these results, the organic material in **GSS$_{95}$** is able to crosslink 5–6% of the sulfur present in the material whereas the **GES** in **GSS$_{90}$** crosslinks <1% of the available sulfur. This data is also consistent with the cross-linked portion of the material being much more localized with significantly shorter sulfur catenates. A similar trend was observed in **OSS$_x$** materials where **OSS$_{95}$** was able to incorporate more sulfur into the crosslinked network but on a much smaller scale (9.5 and 8.3 wt% for **OSS$_{95}$** and **OSS$_{90}$**, respectively, ESI,† Table S3). The trend is readily rationalized because although both **OS** and **GES** have a low degree of olefin modification, **GES** has very concentrated densities of olefins due to the necessary proximity of geraniol-derived olefins and the octenyl succinate derived olefin. IR analysis of the CS_2 insoluble fractions revealed more sulfur-derived scattering seen as baseline absorbance in **GSS$_{95}$** and a worse signal to noise compared to **GSS$_{90}$** further substantiating this hypothesis (ESI,† Fig. S10).

Although the low degree of substitution did not allow visualization of differences between GSS_{90} and GSS_{95} by IR spectroscopy, differences were evident from scanning electron microscopy with elemental mapping by energy dispersive spectroscopy (SEM-EDS, ESI,† Fig. S11) clearly revealing regions of crosslinked organic material. In both GSS_x materials the organic fraction of the material was well dispersed within the material but agglomerated into small regions throughout the material. Consistent with what was suggested from thermal and fractionation results, the clusters of organic material were larger and more plentiful in GSS_{90} than was observed for GSS_{95}.
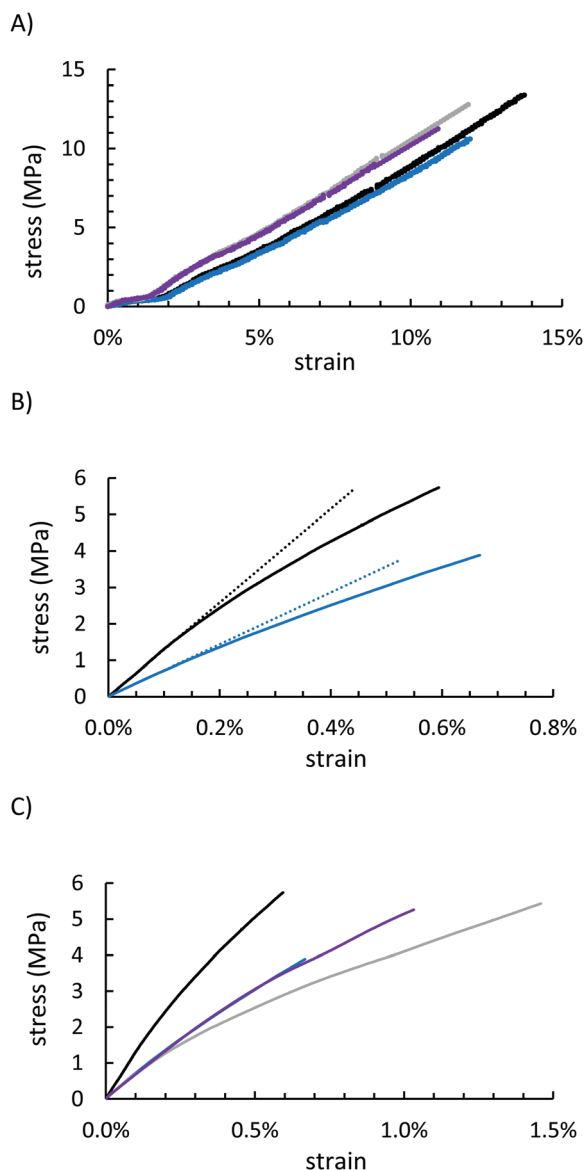
Fig. 6 Mechanical data for GSS_{95} (black), GSS_{90} (blue), OSS_{95} (gray), and OSS_{90} (purple). Compression data for all four materials reveal that each class of materials behaved similarly but with different ultimate strengths where the 95 wt% materials performed better (A). Flexural data for GSS_{95} and GSS_{90} (solid lines) plotted with their flexural moduli (dotted lines) (B), revealing significantly higher strength and stiffness of GSS_{95} relative to GSS_{90} and all four materials plotted together (C).

Mechanical properties of GSS_x were assessed by mechanical test stand analysis (compressive strength) and by dynamic mechanical analysis (DMA, flexural strength). Because GSS_x materials are morphologically more like a particle-reinforced crystalline material relative to a polymeric material, they deformed entirely plastically before breaking under a compressional stress (Fig. 6A and Table 1). The more uniform dispersion of organic material in the network of GSS_{90} allowed for better reproducibility but provided less strength than the minimal filling observed in GSS_{95} (13.4 ± 2.1 MPa and 10.6 ± 0.7 MPa for GSS_{95} and GSS_{90}, respectively). This trend was nearly identical in the OSS_x series. Relative to OSS_x materials, however, GSS_x materials were less stiff but GSS_{95} was found to be the strongest material. This fact can similarly be explained by the differences in morphology between the two materials. While OSS_x has long crosslinks and more interaction between the domains, GSS_x is essentially acting as a particle-reinforced network of sulfur. Recently-reported HSMs comprising variously-sized lignocellulosic particles and sulfur show similar behaviours.[79]

Under a flexural deformation (Fig. 6B and C), GSS_{90} and OSS_{90} behaved very similarly except that GSS_{90} broke at 1.5 MPa less stress than did OSS_{90}. In general, HSMs having a lower percentage of less CS_2-extractable free sulfur are able to withstand flexural stresses-typically leading to a trend where incorporation of a higher feed ratio of the organic component produces a stronger material. This trend was not observed for GSS_x materials. Although they contained nearly identical amounts of free-sulfur, GSS_{95} significantly outperformed GSS_{90} in the flexural strength test, making it the stiffest and strongest of all of the starch-sulfur vulcanized composites, while also having a high moduli of resilience and reasonable toughness (Table 1 and ESI,† Table S3). This interesting deviation from the general trend observed for HSMs may be attributable to the morphological uniqueness of this series of materials.

Under a flexural deformation (Fig. 6B and C), GSS_{90} and OSS_{90} behaved very similarly except that GSS_{90} broke 1.5 MPa before OSS_{90}. The trend observed in OSS_x materials where the material that was less CS_2 soluble (*i.e.* more of the material was part of the crosslinked network), the better the material was able to withstand flexural stresses. Because GSS_{95} was less CS_2 soluble, it outperformed GSS_{90}, and quite significantly, making it the stiffest and strongest material of the series while also having a high moduli of resilience and toughness (Table 1).

Table 1 Flexural analysis data for sulfur−starch composite materials

	GSS_{95}	GSS_{90}	OSS_{95}	OSS_{90}
Strength (MPa)	5.7	3.9	5.4	5.3
Limit of linearity (%)[a]	0.15	0.16	0.13	0.31
Limit of linearity (MPa)[a]	1.9	1.1	0.9	2.0
Flexural modulus (MPa)	1290	710	690	660
Modulus of resilience (kPa)[b]	1.5	0.9	0.6	3.2
Toughness (kPa)[c]	19.1	13.9	42.9	30.2

[a] Defined as a deviation of 0.05 MPa from the linear region. [b] The area under the linear region up to the limit of linearity (%). [c] The area under the entire stress–strain curve.

Conclusions

Herein is reported a green method to esterify octenyl succinate-modified starch, a commercial food additive, to increase its degree of olefination by 2-fold in new derivative **GES**. The significant increase in crosslinkable sites paired with the high local density of reactive sites allowed access to a novel morphological regime of biopolymer–sulfur composites produced by inverse vulcanization of the modified starch with elemental sulfur. These vulcanized composites exhibited unprecedentedly low sulfur ranks which ultimately resulted in the materials taking the form of particle-reinforced networks, analogous to common structural materials such as cement. It was found that vulcanization of bulk sulfur with only a 5 wt% feed ratio of modified starch **GES**, led to materials with excellent stiffness and strength under a flexural and compressional deformation. The trends observed herein between **OSS**$_x$ and **GSS**$_x$ materials seems to suggest that morphology can be controlled depending on the regiochemistry of biopolymer modification prior to its vulcanization. In cases where the crosslinkable sites are necessarily close to one another, short sulfur catenates inevitably form. In this regime, high-strength materials can be produced even with minimal modification, thereby improving the sustainability of the process by decreasing chemical, energy, and waste considerations expenditures while also decreasing the time to material homogenization. These factors ultimately lead to a less expensive and more green cement-surrogate, thus informing future material design.

Experimental

General considerations

Fourier transform infrared spectra were obtained using an IR instrument (Shimadzu IRAffinity-1S) with an ATR attachment. Scans were collected over the range 400–4000 cm^{-1} at ambient temperature with a resolution of 8. TGA was recorded (Mettler Toledo TGA 2 STAR^e System) over the range 20–800 °C with a heating rate of 10 °C min^{-1} under a flow of N$_2$ (100 mL min^{-1}). Each measurement was acquired in duplicate and presented results represent an average value. DSC was acquired (Mettler Toledo DSC 3 STAR^e System) over the range 60 to 150 °C with a heating rate of 5 °C min^{-1} under a flow of N2 (200 mL min^{-1}). Each DSC measurement was carried out over five heat–cool cycles. Each measurement was acquired in triplicate to ensure consistent results were obtained.

DMA was performed (Mettler Toledo DMA 1 STAR^e System) in single cantilever mode. DMA samples were cast from silicone resin moulds (Smooth-On Oomoo$^{®}$ 30 tin-cure). Samples were manually sanded to ensure uniform dimensions of approximately 15 × 8 × 1.5 mm but due to instrumental limitations (maximum force of 10 N), each sample differed slightly in thickness to obtain a stress at break. Sample dimensions were measured with a digital calliper with 0.01 mm resolution. Clamping was done by hand due to the samples' brittleness. The force was varied from 0 to 10 N with a ramp rate of 0.2 N min^{-1} measured isothermally at 25 °C.

Carbon disulfide extractions were performed by suspending 0.3 g of finely ground material (measured to 0.0001 g) in 20 mL of CS$_2$, allowing the solid to settle for 30 minutes, pipetting off the supernatant into a separate vial, and adding another 20 mL of CS$_2$. This process was repeated an additional 3 times so that a total of 5 washes was performed. The residual CS$_2$ was evaporated under a flow of N$_2$, and each vial was weighed to determine the fraction that was soluble (collected as supernatant) or insoluble (remained in the initial vial). This process was performed in duplicate because of unanticipated results yielding identical results both times.

Compressional analysis was performed on a Mark-10 ES30 test stand equipped with a M3-200 force gauge (1 kN maximum force with 1 N resolution) with an applied force rate of 3–4 N s^{-1}. Compression cylinders were cast from silicone resin moulds (Smooth-On Oomoos 30 tin-cure) with diameters of approximately 6 mm and heights of approximately 10 mm. Samples were manually sanded to ensure uniform dimensions and measured with a digital calliper with 0.01 mm resolution. Compressional analysis was performed in triplicate and results were averaged.

Powder X-ray diffraction samples were placed on zero background sample holders and analysed using a Rigaku Ultima IV diffractometer with Cu Kα radiation (l = 1.5406 Å). Data were collected from 5–65 degrees in 2-theta at a rate of 0.5 degree per minute with a sampling interval of 0.02 degrees. Crystallinity calculations were performed by integrating amorphous peaks at 19.01 and 26.43° and crystalline peak integrations at 12.00, 15.35, 17.21, 18.10, and 23.16° as is reported in the literature.[80]

SEM was acquired on a Schottky Field Emission Scanning Electron Microscope SU5000 operating in variable pressure mode with an accelerating voltage of 15 keV. NMR was conducted based on literature procedures.[81] GES or OS was suspended in DMSO-d6 (12.5 mg mL^{-1}) and sonicated for 2 hours at 70 °C. Molecular sieves (4 Å) were added and the samples were left over night. Proton NMR spectra were acquired on a Bruker NEO-300 MHz at room temperature and data was processed with TopSpin 4.0.6 software. All spectra reported were calibrated to the solvent peak at 2.50 ppm.

Author contributions

The author primarily responsible for particular credit roles are provided here. Moira K. Lauer: data curation, formal analysis, investigation, validation, roles/writing – original draft. Andrew G. Tennyson: resources. Rhett C. Smith: conceptualization, funding acquisition, methodology, formal analysis, resources, supervision, writing – review and editing.

Conflicts of interest

There are no conflicts to declare.

Acknowledgements

Notes and references

1 P. A. Arias, N. Bellouin, E. Coppola, R. G. Jones, G. Krinner, J. Marotzke, V. Naik, M. D. Palmer, G.-K. Plattner, J. Rogelj, M. Rojas, J. Sillmann, T. Storelvmo, P. W. Thorne, B. Trewin, K. A. Rao, B. Adhikary, R. P. Allan, K. Armour, G. Bala, R. Barimalala, S. Berger, J. G. Canadell, C. Cassou, A. Cherchi, W. Collins, W. D. Collins, S. L. Connors, S. Corti, F. Cruz, F. J. Dentener, C. Dereczynski, A. D. Luca, A. D. Niang, F. J. Doblas-Reyes, A. Dosio, H. Douville, F. Engelbrecht, V. Eyring, E. Fischer, P. Förster, B. Fox-Kemper, J. S. Fuglestvedt, J. C. Fyfe, N. P. Gillett, L. Goldfarb, I. Gorodetskaya, J. M. Gutierrez, R. Hamdi, E. Hawkins, H. T. Hewitt, P. Hope, A. S. Islam, C. Jones, D. S. Kaufman, R. E. Kopp, Y. Kosaka, J. Kossin, S. Krakovska, J.-Y. Lee, T. M. J. Li, T. K. Maycock, M. Meinshausen, S.-K. Min, P. M. S. Monteiro, T. Ngo-Duc, F. Otto, I. Pinto, A. Pirani, K. Raghavan, R. Ranasinghe, A. C. Ruane, L. Ruiz, J.-B. Sallée, B. H. Samset, S. Sathyendranath, S. I. Seneviratne, A. A. Sörensson, S. Szopa, I. Takayabu, A.-M. Treguier, B. V. D. Hurk, R. Vautard, K. V. Schuckmann, S. Zaehle, X. Zhang and K. Zickfeld, *Climate Change 2021: The Physical Science Basis. Contribution of Working Group I to the Sixth Assessment Report of the Intergovernmental Panel on Climate Change*, ed. V. Masson-Delmotte, P. Zhai, A. Pirani, S. L. Connors, C. Péan, S. Berger, N. Caud, Y. Chen, L. Goldfarb, M. I. Gomis, M. Huang, K. Leitzell, E. Lonnoy, J. B. R. Matthews, T. K. Maycock, T. Waterfield, O. Yelekçi, R. Yu and B. Zhou, Cambridge University Press, 2021.
2 K. L. Scrivener, V. M. John and E. M. Gartner, *Cem. Concr. Res.*, 2018, **114**, 2–26.
3 R. M. Andrew, *Earth Syst. Sci. Data*, 2018, **10**, 195–217.
4 M. Dehestani, E. Teimortashlu, M. Molaei, M. Ghomian, S. Firoozi and S. Aghili, *Data Brief*, 2017, **13**, 137–144.
5 E. D. Weil, *Phosphorus, Sulfur Silicon Relat. Elem.*, 1991, **59**, 325–340.
6 U.S. Department of Transportation, Extension and Replacement of Asphalt and Cement with Sulfur (FHWA-RD-78-95), 1978.
7 I. Deme, Sulphur Pellet Comprising H$_2$S-Suppressant for Asphalt Paving Mixture, WO2004-EP53357, 2005.
8 I. Deme, *Adv. Chem. Ser.*, 1978, **165**, 172–189.
9 J. E. Gillott, I. J. Jordaan, R. E. Loov, N. G. Shrive and M. A. Ward, *Adv. Chem. Ser.*, 1978, **165**, 98–112.
10 G. J. Kennepohl and L. J. Miller, *Adv. Chem. Ser.*, 1978, **165**, 113–134.
11 M. Al-Ansary, E. Masad and D. Strickland, *Adv. Gas Process.*, 2010, **2**, 121–130.
12 A. Taylor, N. Tran, R. May, D. Timm, M. Robbins and B. Powell, *J. Assoc. Asphalt Paving Technol.*, 2010, **79**, 403–441.

13 D.-y. Lee, *Prod. R&D*, 1975, **14**, 171–177.
14 S. Gwon, E. Ahn and M. Shin, *Composites, Part B*, 2019, **162**, 469–483.
15 S. Gwon, S.-Y. Oh and M. Shin, *Constr. Build. Mater.*, 2018, **181**, 276–286.
16 S. Gwon and M. Shin, *Constr. Build. Mater.*, 2019, **228**, 116784.
17 P. Szajerski, A. Bogobowicz and A. Gasiorowski, *J. Hazard. Mater.*, 2020, **381**, 121180.
18 M. Lewandowski and R. Kotynia, *MATEC Web Conf.*, 2018, **219**, 3006.
19 S. Mohammed and V. Poornima, *Mater. Today: Proc.*, 2018, **5**, 23888–23897.
20 W. J. Chung, J. J. Griebel, E. T. Kim, H. Yoon, A. G. Simmonds, H. J. Ji, P. T. Dirlam, R. S. Glass, J. J. Wie, N. A. Nguyen, B. W. Guralnick, J. Park, A. Somogyi, P. Theato, M. E. Mackay, Y.-E. Sung, K. Char and J. Pyun, *Nat. Chem.*, 2013, **5**, 518–524.
21 Y. Zhang, R. S. Glass, K. Char and J. Pyun, *Polym. Chem.*, 2019, **10**, 4078–4105.
22 T. S. Kleine, R. S. Glass, D. L. Lichtenberger, M. E. MacKay, K. Char, R. A. Norwood and J. Pyun, *ACS Macro Lett.*, 2020, **9**, 245–259.
23 P. Yan, W. Zhao, B. Zhang, L. Jiang, S. Petcher, J. A. Smith, D. J. Parker, A. I. Cooper, J. Lei and T. Hasell, *Angew. Chem., Int. Ed.*, 2020, **59**, 13371–13378.
24 M. J. H. Worthington, R. L. Kucera and J. M. Chalker, *Green Chem.*, 2017, **19**, 2748–2761.
25 J. M. Chalker, M. J. H. Worthington, N. A. Lundquist and L. J. Esdaile, *Top. Curr. Chem.*, 2019, **377**, 1–27.
26 T. Hasell, D. J. Parker, H. A. Jones, T. McAllister and S. M. Howdle, *Chem. Commun.*, 2016, **52**, 5383–5386.
27 M. W. Thielke, L. A. Bultema, D. D. Brauer, P. Theato, B. Richter and M. Fischer, *Polymers*, 2016, **8**, 1–9.
28 D. J. Parker, H. A. Jones, S. Petcher, L. Cervini, J. M. Griffin, R. Akhtar and T. Hasell, *J. Mater. Chem. A*, 2017, **5**, 11682–11692.
29 A. M. Abraham, S. V. Kumar and S. M. Alhassan, *Chem. Eng. J.*, 2018, **332**, 1–7.
30 H.-K. Lin, Y.-S. Lai and Y.-L. Liu, *ACS Sustainable Chem. Eng.*, 2019, **7**, 4515–4522.
31 Y. Chen, A. Yasin, Y. Zhang, X. Zan, Y. Liu and L. Zhang, *Materials*, 2020, **13**, 632.
32 A. D. Tikoalu, N. A. Lundquist and J. M. Chalker, *Adv. Sustainable Syst.*, 2020, **4**, 1900111.
33 J. J. Griebel, S. Namnabat, E. T. Kim, R. Himmelhuber, D. H. Moronta, W. J. Chung, A. G. Simmonds, K.-J. Kim, J. van der Laan, N. A. Nguyen, E. L. Dereniak, M. E. MacKay, K. Char, R. S. Glass, R. A. Norwood and J. Pyun, *Adv. Mater.*, 2014, **26**, 3014–3018.
34 S. Namnabat, J. J. Gabriel, J. Pyun and R. A. Norwood, *Proc. SPIE*, 2014, **8983**, 89830D.
35 S. Namnabat, J. J. Gabriel, J. Pyun, R. A. Norwood, E. L. Dereniak and J. van der Laan, *Proc. SPIE*, 2014, **9070**, 90702H.
36 J. J. Griebel, N. A. Nguyen, S. Namnabat, L. E. Anderson, R. S. Glass, R. A. Norwood, M. E. MacKay, K. Char and J. Pyun, *ACS Macro Lett.*, 2015, **4**, 862–866.